

Spatial profiles of interelectrode electron density in direct current superposed dual-frequency capacitively coupled plasmas

Yoshinobu Ohya,^{1,2} Kenji Ishikawa,^{1,*} Tatsuya Komuro,¹ Tsuyoshi Yamaguchi,¹ Keigo Takeda,¹ Hiroki Kondo,¹ Makoto Sekine,¹ and Masaru Hori¹

¹ Nagoya University, Furo-cho, Chikusa, Nagoya, Aichi 464-8603, Japan

² Tokyo Electron Limited, Kurokawa, Miyagi 981-3629, Japan

* E-mail: ishikawa.kenji@nagoya-u.jp

We present experimentally determined spatial profiles of the interelectrode electron density (n_e) in dual-frequency capacitively coupled plasmas in which the negative direct current (dc) bias voltage (V_{dc}) is superposed; in the experiment, 13 MHz (P_{low}) was applied to the lower electrode and 60 MHz (P_{high}) to the upper electrode. The bulk n_e increased substantially with increases in the external power, P_{high} , P_{low} , and with increases in V_{dc} . When P_{low} was insufficient, the bulk n_e decreased as the V_{dc} bias increased. The bulk n_e increased due to its dependence on V_{dc} , especially for $|V_{dc}| > 500$ V. This may correspond to the sheath voltages (V_s) of the lower electrode. The n_e values in front of the upper electrode were coupled with the V_{dc} : the V_{dc} dependence first decreased and then increased. The dc currents (I_{dc}) of the upper electrode were collected when a large P_{low} was applied. The value of I_{dc} at the threshold value of $V_{dc} \approx V_s$ (e.g., -500 V) increased with an increase in n_e . When $|V_{dc}|$ exceeded the threshold, the spatial n_e profile and the I_{dc} dependence were changed relative to the electrical characteristics of the dc superposition; this led to a change in the location of the maximum n_e , the width of the area of n_e depletion in front of the electrodes, and a

transition in the electron heating modes.

1. Introduction

Using halogen-containing gases for sputter etching increases the rate of etching; this was first described by Hosokawa *et al.*[1] This technique is also known as reactive-ion etching,[2] and it is widely used for capacitively coupled plasma (CCP); it is indispensable for fabricating ultralarge-scale integrated circuits (ULSIs).[3] In a conventional CCP, two parallel-plate-type electrodes are used, and radio-frequency (rf) power is applied, either independently or at the same time. Here, one of the electrodes (the “lower” electrode) is used to set up a wafer, and the counter electrode (the “upper” electrode) is powered for plasma generation.[4-17] The ion energy and flux at the electrodes can be controlled separately by discharges driven at different frequencies: the high-frequency voltage controls the charged particle density, and the low-frequency voltage controls the acceleration of the ions in the sheaths. This type of reactor is referred to as a dual-frequency CCP reactor.[7,8] Because a large wafer size and high excitation frequency are used, it is necessary to ensure that the plasma etching is uniform. Recently, in commercial reactors, a negative direct current (dc) voltage has been superposed to the upper electrode in parallel-plate-type CCPs [18]. The dc-superposed CCP etcher meets these requirements; it improves the uniformity and suppresses the profile distortions due to small features, which are the most likely cause of surface charging effects.[19,20] Therefore, the effects of dc superposition need to be further analyzed in a comprehensive way. In a previous paper, we demonstrated that the electron density increases as the voltage of the dc superposition increases [12]; this

increase with the dc voltage has also been shown for the radical density [11].

Here, we consider the characteristics of a dual-frequency CCP, both with and without dc superposition. We measured the electron densities in a dual-frequency CCP with a superposed negative dc voltage and under various conditions. The electron density is considered to be the most important parameter when evaluating the characteristics of the plasma. In our experiments, we considered the controllable parameters to be the very-high-frequency (vhf) power, the rf power, and the negative dc bias. The observed characteristics will be discussed in terms of the dc self-bias, dc superposition, electron heating, and surface charge neutralization.

2. Background

Before discussing our results, we will briefly summarize the background of dc superposed CCPs, with respect to 1) the relationship of *self-bias voltages* on CCP discharges to geometrical and electrical symmetry, 2) *dc superposition* onto the CCP electrode, 3) *electron heating* and losses to the wall, and 4) *surface charging neutralization* and electron shading effects inside small features.

First, the self-bias voltage of CCP discharges is a key feature of the electrical behavior of a CCP discharge system. The sheath model was an early (1972) attempt to understand the self-bias voltage.[21] The development of the dc self-bias voltage can be modeled using the sheath capacitances of the self-consistent sheaths formed in front of each electrode. Simply put, the CCP discharge systems are modeled by representing the sheath as a capacitance. The dc self-bias, V_s , that is developed is expressed as $V_s = (C_p - C_g)/(C_p + C_g)V_{rf}$, where C is the capacitance, the subscripts p and g stand

for “powered” and “grounded” electrodes, respectively, and V_{rf} is the applied rf voltage.[22] Note that V_s is generated when there is an asymmetric discharge. When there is a single-frequency discharge and one electrode is powered and the other is grounded, this leads to high sheath voltages and high ion energies at the smaller electrode.[23]

In the 1990s, it was accepted that in dual-frequency CCPs, the discharges have separate functions: the high-frequency voltage sustains the plasma, and the low-frequency voltage controls the acceleration of the ions in the sheaths.[4-6] For the discharges of dual-frequency CCPs, the equivalent circuit is obtained by adding the blocking capacitor and another rf source to the lower electrode, as shown in Fig. 1(b). The modified circuit has two blocking capacitors, C_{lower} and C_{upper} . It is important to note that the capacitances are divided by the application of voltages on the sheath capacitances, C_{sh} . This voltage balance model can also be used to understand the electrical characteristics.

In the 2000s, Czarnetzki *et al.* introduced a more detailed voltage balance model to explain the electrical behavior of the multiple-frequency CCP discharges.[23] The CCP discharges are symmetric, i.e., the surface areas of the powered electrode, A_p , and the grounded electrode, A_g , are either identical ($A_p = A_g$) or asymmetric ($A_p \neq A_g$).[23] A schematic of the equivalent circuit with potential Φ is shown in Fig. 1(a). The voltages at each node are $\bar{V}_{\sim}(t) = \bar{V}_C[\tilde{q}] + \bar{V}_{sp}[\tilde{q}] + \bar{V}_{sg}[\tilde{q}] + \bar{V}_b[\tilde{q}]$, where \bar{V}_{\sim} is the applied voltage waveform, \bar{V}_C is the blocking capacitor, \bar{V}_{sp} and \bar{V}_{sg} are the voltage drops across the powered and grounded electrode, respectively, \bar{V}_b is the bulk plasma voltage, and $\tilde{q} = q(t) = Q(t)/Q_0$ is the normalized space charge in the sheath as a function of time.[23] The positive charges are in the sheath at each of the electrodes,

and the normalized total charge is located inside the sheaths; thus, we have $q_t(t) = q(t) + q_{sg}(t)$, where q_{sg} is the normalized positive space charge in the sheath at the ground electrode.[23] It is worth noting that positively and negatively charged particles are lost independently at the walls, and the electronegative electron flux Γ_e must be balanced by the electropositive ion flux Γ_i on the floating electrode. Thus, within a single frequency period, q_t is determined by the continuous loss of positive ions to the electrode, due to the Bohm fluxes [24,25], and by the instantaneous loss of electrons to the electrode at the phases of sheath collapse. A constant current develops throughout the plasma, and an additional electric field is necessary to equalize the current. The drops in voltage across the sheath are associated with these capacitances, and they can be represented by an integral of charges, based on Gauss' law.[26]

Recently, it has been proposed that the electrical asymmetry effect (EAE) can generate a variable V_s by controlling the phase shifts between multiple frequencies.[23] In details, within the rf period, sheath voltages instantaneously oscillated. The maximum voltages were linked via the symmetry parameter $\varepsilon = \left| \frac{\max V_{sg}}{\max V_{sp}} \right| \approx \left(\frac{A_p}{A_g} \right)^2 \frac{\bar{n}_{sp}}{\bar{n}_{sg}} \left(\frac{Q_{mg}}{Q_{mp}} \right)^2$, where \bar{n}_s is the spatially averaged ion density in the sheath, and Q_m is the maximum charge in the given (g or p) sheath.[23] Thus, V_s can be written as $V_s = \frac{\phi_{max} + \varepsilon \phi_{min}}{1 + \varepsilon}$, where ϕ is the potential at the sheath.[27] Simply put, V_s is due to the unbalanced charges of the two electrodes.[28] We note that electropositive ions respond to the time-averaged electric field, and electrons follow the instantaneous electric field.[29] The model for the time-averaged integral of positive charges in the sheaths, $s(t)$, is based on the instantaneous position of the boundary between the sheath and the plasma; s_{max} is the maximum extent of the sheath.[25]

Ideally, the temporally averaged mean sheath voltage V_s is equal to the difference between the absolute values of the period-averaged sheath voltages, $V_s = |\langle \phi_s^{(lower)} \rangle| - |\langle \phi_s^{(upper)} \rangle|$. A schematic of the simplified plasma density (n_e) and ion density (n_i) profiles is presented in Fig. 1(c). The maximum sheath extent (as either thickness or width) is usually on the order of millimeters or less and on the order of tens of pascals or less.

Next, we note that it has been argued that the drop in voltage of the sheath, V_s , is controlled by the application of the dc voltage to the CCP electrode. The setup in a previous study considered two configurations of the applied dc and rf power.[8] In the first, the combination configuration, the electrodes are operated by separate rf and dc power supplies; this configuration can be further classified by having a grounded or floating rf electrode. In the second configuration, the dc is superposed onto the rf electrode. The configurations used in selected references are presented in Table I. In 1985, Kohler *et al.* first described the dc superposition and reported that the potential was slightly modified by the superposition of a dc voltage [22]. The combination of rf and dc discharge sources was first reported by Yamamoto and Okuda in 1956,[30] and later by Hassan and Fujita.[31] Thereafter, in the late 2000s, several researchers reported computational results that showed that when a negative dc voltage was applied to the electrode, the sheath structure was superposed electromagnetically by a combination of a dc sheath and an rf sheath.[32-35]

The computational studies were limited in the high-pressure regimes and dealt with the collisional discharges. For low-power discharges at low pressures, the electron heating mechanism in collisionless cases is dominated by stochastic (or hard-wall) heating from electrons interacting with the moving high-voltage rf sheath.[36] A

high-voltage sheath is formed and driven by the combination of the dc and rf source, $V = V_{rf} + V_{dc}$. The time-varying electron density within the sheath was calculated by using the ion current density; a large dc bias was applied to the sheath, and Child's law was then used to calculate the electrical circuit across the sheath .[32,33] In addition, the bombardment of ions accelerated by the high-voltage sheath will enhance the emission of secondary electrons, and the electrons generated on the electrode surface will accelerate back into the plasma, thereby increasing the plasma density.[32-35] The electron heating mechanisms in the discharges sustained by the application of large rf voltages at low pressure have received much attention, in particular, in the case of dc superposition.

Third, the plasma is sustained by the balance between the electron heating and the losses to the wall. The particle and energy balance is expressed by the bulk ionization and total surface loss.[36] In the bulk plasma, the momentum transfer due to collisions between oscillating electrons and neutral particles absorbs the time-averaged power; this is known as ohmic heating. The discharges sustain this bulk heating mode, and so the current throughout the plasma is relatively low; this is known as the low-current α mode.[37] In the low-pressure regime, the electrons reflected by the large decelerating field due to the moving high-voltage sheath obtain power from the oscillating sheath; this is known as stochastic heating.[36] The transition between modes, ohmic heating due to collisions, and collisionless stochastic heating have been reported previously.[38]

For discharges at low power and at low pressures, collisionless heating will primarily be absorbed by the external power supply. Godyak and Lieberman discovered that the dominant mechanism for collisionless heating was the interaction of stochastic

(or hard-wall) heating with electrons [39,40]. At low pressure, collisionless stochastic heating is dominant, and the heating due to collisions is not significant.

In contrast to stochastic heating, in collisionless heating, the ions strike the electrode. Secondary electrons are generated and are accelerated back into the plasma. The current throughout the plasma is thus relatively high; this is known as the high-current γ mode.[37]

In general, secondary electrons are not produced by ionization at low pressures; however, Godyak *et al.* points out that at around 300 Pa and with high ion energy, the plasma is sustained by the secondary electrons alone; this is known as the α - to γ -mode transition.[38-40] In 1958, Levitskii was the first to establish the α - to γ -mode transition.[37,41] Subsequently, the α - to γ -mode transition was reported by Lisovski *et al.*[42] and Donko *et al.*[43]

When there are multiple excitation frequencies, it has been proposed that there is a mode transition from ohmic to stochastic heating. Zhang *et al.* presented results for the transition from heating dominated by a dual-frequency stochastic mode to one dominated by direct current, and they argued that this induced the emission of secondary electrons [44,45]. For simplicity, they assumed that the transition was to the nontraditional γ -mode and the dc superposition was limited. At present, the consensus is that with the dc superposition, these behaviors are similar to the dc discharges; this type of heating is known as the γ mode. Under these conditions, the n_e profiles can be considered in terms of the sheath voltage, which is modulated by the dc superposition.

Fourth, in particular, with plasma etching technology, the electron shading effects inside small features are determined by the precise control of the etched features.[46] In 1990, Hashimoto reported that the positively charged ions strike the

inside of small features due to the acceleration of the time-averaged negative electric field that builds up toward the surface; however, the negatively charged electrons are prevented from reaching the bottom of the feature, and this results in thermal motions without an accelerating field.[47,48] At the bottom surface of a small feature, localized charging is due to the arrival and deflection of electrons within the feature, and thus the shape profiles are distorted; this results in commonly seen artifacts, such as trenching, bowing, notching, and twisting.[46] Thus, some researchers believe that the accelerated, ballistic transport of electrons may neutralize the charge that is built up on the bottom surface of a feature.[19-21] Wang and Kushner reported computational results obtained from the hybrid plasma equipment model (HPEM).[43,44] They calculated the behavior of secondary electron emissions from Ar when the lower electrode received power at either 10 MHz or 2 MHz, and the upper electrode received dc augmentation (also called dc superposition). The computational results showed that highly energetic secondary electrons impinged onto the lower electrode surface, and that this increased the random occurrence of holes or trench shapes that deviated from the vertical [49,50]. The secondary electrons that are emitted by the upper electrode irradiate the lower electrode, resulting in neutralization. This is believed to neutralize the charged surface; that is, the secondary electrons accelerate with the negative dc potential and neutralize the inside of the microstructure.

The ballistic transport of secondary electrons through a bulk plasma was reported by Khrabrov *et al.* The electron velocity distribution function (EVDF) of the lower electrode has not yet been clarified for this setup.[51] The secondary electrons originating from the dc-biased surface were accelerated to an energy nearly equal to the bias potential, and another portion of the electrons emitted from the rf electrode

eventually bounced between the sheaths.[51] Xu *et al.* reported that the ballistic electrons originated as secondary electrons produced by ion and electron bombardment of the electrodes. The energy distribution of the ballistic electrons peaked at the value of the negative bias applied to the dc electrode.[52] Diomeda *et al.* reported that the EVDF striking the substrate extended all the way to $V_{rf} + |V_{dc}|$, the sum of the peak rf voltage and the absolute value of the applied dc bias.[53] In either the combination or superposition setup, the secondary electron emissions are determined by the EVDF features involving ballistic transport of electrons along the developed large sheath potentials. As a consequence, the secondary electrons accelerate back into the plasma, and ballistic transport carries them through the bulk plasma, where they impinge inside the small feature; this results in a possible neutralization of the effect of the local surface charge.

We have considered the mechanism that determines the interelectrode electron density profiles, and we summarized the background of the dc superposed CCPs with respect to 1) self-biased voltages, 2) dc superposition and dc combination, 3) electron heating and losses, and 4) surface charge neutralization. We evaluated the electron densities by balancing the surface losses of electrons with the ionizations, since the realistic discharges are too complex to understand; we do not have enough information to elucidate the mechanism that determines the electron density or the spatial density distributions.

3. Experiment Setup

A surface wave (SW) probe (also known as a plasma absorption probe, PAP)

was used in this study [12,54] to measure the actual electron density (n_e) in conventional fluorocarbon plasmas [54-61]. The SW probe measures the absorption of a surface wave exiting from the head of a dielectric-covered probe [54]. We emphasize that the SW probe is completely covered by dielectrics that surround the conducting antenna, and thus it differs in this way from other resonance probes, such as cut-off probes.[62] The surface waves propagate in the microwave frequency range, and the signal can be detected by a network analyzer.

A Langmuir electrostatic probe is commonly used to measure n_e . [36] Unfortunately, this probe cannot be used with fluorocarbon plasmas or with industrial fluorocarbon CCP etchers; in those situations, an insulating film is deposited onto the probe surface, and this interrupts measurement of the electrical current. Although microwave interferometry can be used to measure n_e , in spite of the deposition of a film, only a line-averaged density can be measured. Thus, the SW probe is better for the purposes of this study.

Figure 2 shows a schematic of a commercially available dual-frequency (60 MHz/13.56 MHz) CCP apparatus equipped with an SW probe measurement system [61]. A quartz tube with an outer diameter of 5 mm was inserted into a port in the cylindrical chamber wall. The SW probe head consists of a 5-mm-long monopole antenna at the end of a coaxial cable with a diameter of 0.8 mm. Microwave power of ~ 1 mW was fed to the probe head from a network analyzer (Agilent E5071C, possible sweep range between 100 and 8000 MHz), and the frequency varied from 500 MHz to 1500 MHz. The power reflection coefficient Γ was obtained as a function of frequency. The incident power is sharply absorbed at a certain frequency f_{abs} , because a standing mode of the SW resonates at the probe head. The observed absorption frequency f_{abs} (MHz) is

related to the electron density n_e (cm^{-3}) as $n_e = \beta \times 10^4 (f_{abs})^2$, where β is the proportionality constant, which was determined by the plasma oscillation method to be 3.78 for the probe used in our experiments [12].

In measurements of the interelectrode profile, the canted probe head was moved vertically by rotating it with an offset of 20 mm, as shown in Fig. 2(b), and thus the horizontal position changed simultaneously with the vertical position; however, the change in the horizontal position was less than 20 mm, due to the uniformity of n_e . An electrode diameter of 300 mm was sufficiently large to measure the interelectrode n_e profile. The probe had a relatively large diameter (5 mm) in order to obtain spatial profiles with reasonable resolution. The spatial positions were normalized by the interelectrode distance. The positions Z_{center} and Z_{upper} are the center of the plasma bulk and the front of the upper electrode, respectively. Using the spatially resolved measurements, we obtained the spatial profile at 2 mm increments of step height.

The dc current at the upper electrode was measured during discharge; the current density per unit area, I_{dc} , was estimated by dividing the measured current by the area of the upper electrode. We should note that we neglected the nonuniformity of the current; i.e., we only considered the total current flowing through the entire upper electrode.

A gas mixture was introduced into the chamber at the upper electrode. The aperture had a diameter of 30 cm, and it could be biased for a negative dc voltage. The gas consisted of $\text{C}_4\text{F}_8/\text{N}_2/\text{Ar}$ at flow rates of 10/100/800 standard cc per minute (sccm). The gas composition was the same as that commonly used for reactive ion etching. The amount of electronegative C_4F_8 could affect the plasma parameters,[63,64] but we are not interested in analyzing the electronegativity. The gas flow rates were controlled by a

mass-flow controller, and the total pressure was stabilized at 5.33 Pa (40 mTorr) by an automatic pressure controller. The measurements were performed under standard conditions: vhf P_{high} of 0, 500, 800, 1500, and 2400 W at 60 MHz were applied to the upper electrode; and rf P_{low} of 800, 1500, and 2000 W at 13.56 MHz were applied to the lower electrode, which was a distance of 3 cm from the upper plate. In addition, a dc voltage of 0 to -1200 V was applied to the upper electrode.

4. Experimental Results

4-1. Spatial profile of plasma density in a single-frequency CCP

We first investigated the dependence of the vhf power at the upper electrode without the negative dc bias. We note that the rf power was not applied at the lower electrode, that is, $P_{\text{low}} = 0$ W. This single-frequency CCP discharge is similar to one with a powered upper electrode and a counter lower electrode that is electrically floated.

Figure 3 shows the spatial profiles of the plasma density n_e for different values of P_{high} ranging from 800 to 2000 W. At the center, Z_{center} , the n_e increased with increasing P_{high} . The bulk n_e dependence on P_{high} was nearly linear. In the spatial profiles, we observed a wider depletion width W_s of n_e in front of the lower electrode and a narrower width at the upper electrode. In the spatial profile, n_e was depleted on both sides in front of both the upper and lower electrodes. The width of the depletion may be linked closely with the thickness of the sheath; however, the probe was not large enough to evaluate the spatial resolution. The absolute sheath thicknesses could not be analyzed. Hypothetically, the sheath thicknesses for the lower and upper electrodes were represented by the depletion widths coupled with the capacitances of the external circuit,

because the electron density drop at the lower electrode was larger than that at the upper one. We can provide a qualitative interpretation of the depletion widths: a larger width reflects a smaller capacitance, and this leads to a large voltage drop at the lower electrode.

Figure 4(a) shows the spatial profile of n_e as a function of V_{dc} for the case of dc superposition onto a single-frequency CCP electrode. When P_{low} was not applied and V_{dc} was superposed on P_{high} , the bulk n_e was greatly reduced. The application of a large V_{dc} moved the location of the maximum n_e slightly in the direction of the lower electrode. In the following paragraph, we briefly discuss the reduction in n_e , which was a factor in the previously discussed computational results for a single-frequency CCP with rf and dc bias superposition at the upper electrode and a grounded lower electrode.[32,33]

The dependence of n_e at Z_{center} on V_{dc} is shown in Fig. 4(b). As the dc bias superposition was strengthened to more than $-250 V_{dc}$, the bulk n_e decreased. The n_e depletion widths on both sides of the electrode were balanced when the dc bias applied to the upper electrode was more than $-500 V_{dc}$. This implied that when a lower frequency was applied, the sheath voltage drop at the lower electrode might be approximately $-500 V$. There is a large and asymmetric electrical flow, and thus the electrical currents are unbalanced due to the imbalance between the electron and ion fluxes onto the electrode surfaces; the electrode surface acted as an electron sink when the applied V_{dc} was high.

4-2. Spatial profile of plasma density in a dual-frequency CCP

Figure 5 shows the variation in the n_e profiles as a function of the interelectrode position. In Fig. 5(a), P_{high} was 800 W and P_{low} was 1500 W. When a large $|V_{\text{dc}}|$ (more than 250 V) was applied, the area of highest n_e moved from the side of the upper electrode to the side of the lower electrode. Notably, when a P_{low} of 1500 W was applied, the increase in V_{dc} led to an increase in the bulk n_e . Simultaneously, the bulk n_e profile increased. The depletion width W_s^{upper} in front of the upper electrode was widened slightly, while the W_s^{lower} was narrowed slightly. The rf and dc sheaths combined, and the electrons trapped between the electrodes caused the n_e maximum position to move and the bulk n_e to increase. We estimated that for the vhf/dc sheath, V_s^{upper} was almost -100 V.

As shown in Fig. 5(b), when a relatively high P_{high} of 2000 W was applied to the upper electrode, the bulk n_e was approximately $2.0 \times 10^{11} \text{ cm}^{-3}$, and at the lower electrode, n_e remained constant. When we applied $P_{\text{high}} = 2000$ W and $P_{\text{low}} = 1500$ W, an increase in n_e could be observed at the lower electrode; however, the difference was very small. When a $|V_{\text{dc}}|$ smaller than 250 V ($V_{\text{dc}} > -250$ V) was applied, the bulk n_e increased slightly. When $|V_{\text{dc}}|$ was increased beyond 500 V ($V_{\text{dc}} < -500$ V), the bulk n_e again decreased. When $|V_{\text{dc}}|$ was greater than 800 V ($V_{\text{dc}} < -800$ V), the bulk n_e increased with V_{dc} .

The spatial profile had two modes, depending on whether V_{dc} was large or small. When $|V_{\text{dc}}|$ was large (-800 V and -1000 V), the depletion width in front of the upper electrode W_s^{upper} was wider, and n_e was concentrated at the central position. When P_{high} was 2000 W, V_s^{upper} for the vhf /dc sheath was almost -500 V and V_s^{lower} was almost -250 V. When V_s^{upper} was greater than V_s^{lower} , we postulate that the flux is balanced by the upper electrode, which acts as a wall and absorbs electrons.

Figure 6(a–c) shows the interelectrode n_e at Z_{center} as a function of V_{dc} for different values of P_{high} (from 500 W to 1500 W) and different values of P_{low} (800 W, 1500 W, and 2400 W). As P_{low} increased, the base level of n_e increased approximately in proportion to P_{low} : 1.1, 1.3, $1.5 \times 10^{11} \text{ cm}^{-3}$ for 500, 1500, 2400 W, respectively. $|V_{\text{dc}}|$ increased with P_{high} , and then decreased close to $V_{\text{dc}} \approx -400\text{V}$. The locations of these bumps are indicated by the dotted lines and are labeled Regions II and III (the regions will be further discussed below). The bumps occur in the same region of V_{dc} . As P_{low} increases, the bumps are hidden by the increase in the n_e base level. When $|V_{\text{dc}}|$ is large, the n_e dependence increases linearly with V_{dc} , and the range of V_{dc} is labeled Region IV when $|V_{\text{dc}}|$ is high and P_{low} has decreased.

For simplicity, we divide the observed V_{dc} into four regions, determined by the dependence of n_e on V_{dc} . When $|V_{\text{dc}}|$ is smaller than -300 V , n_e is not dependent on V_{dc} (Region I). Then, n_e increases linearly with P_{high} . However, when $|V_{\text{dc}}|$ is large ($V_{\text{dc}} < -600 \text{ V}$), the V_{dc} dependence of n_e is nearly linear, regardless of the size of P_{high} (Region IV). When $|V_{\text{dc}}|$ is large, the bulk n_e increases proportionally with $|V_{\text{dc}}|$. In between Regions I and IV, the V_{dc} dependence displays bumps. There are two types of bump: upward when $|V_{\text{dc}}|$ is smaller (Region II), and downward when $|V_{\text{dc}}|$ is larger (Region III). Interestingly, as P_{high} decreases, the bumps in the V_{dc} dependence weaken and disappear. In particular, in the dual-frequency CCP, the n_e dependence on V_{dc} displays the characteristic bump feature. The voltage at the bump is probably the same as that of the sheath voltage drop at the counter lower electrode, and this may lead to confinement of the bulk plasma. We can estimate that in Region II, $V_s^{\text{upper}} < V_s^{\text{lower}}$, and in Region III, $V_s^{\text{upper}} > V_s^{\text{lower}}$. For the cases shown in Fig. 5(a), P_{low} of 800 W led to $V_s^{\text{lower}} \approx -300 \text{ V}$, and V_s^{upper} ranged from -300 V to -500 V and depended on P_{high} .

To the best of our knowledge, we are the first to report the spatial profile of n_e when dc superposition and P_{high} are applied to the upper electrode and P_{low} is applied simultaneously to the lower electrode. The n_e maximum position in the bulk and the n_e depletion widths W_s in the front of electrodes were determined by various conditions of the external power. We have already shown that these spatial profiles can aid understanding of the effects of dc superposition. As a summary of n_e at Z_{center} , Fig. 6(d) shows the n_e surface in the P_{high} and V_{dc} space.

4-3. Current density of the upper electrode

Next, dc currents that flow through the upper electrode are evaluated by considering their relation to the characteristic bump behavior, which depends on V_{dc} . Figure 7 shows the dependence of (a) I_{dc} and (b) n_e as a function of the dc superposition voltage for P_{high} values ranging from 0 to 2000 W and a constant P_{low} of 1500 W. The values of n_e at Z_{upper} , close to the upper electrode, are plotted.

The conditions were the same as those of Fig. 5(a), where P_{low} was 1500 W and P_{high} was 800 W. When there was no I_{dc} flow at the upper electrode, n_e remained constant, although $|V_{\text{dc}}|$ was more than 100 V ($V_{\text{dc}} < -100$ V). If a P_{high} of 2000 W was applied, n_e remained unchanged, and V_{dc} was below -350 V. If V_{dc} exceeded -350 V, n_e increased and then decreased. Similar bump behaviors were observed at Z_{center} , as discussed above.

For the dependences on P_{high} and V_{dc} when P_{low} was held constant at 1500 W, the behavior of n_e near the upper electrode is shown in Fig. 7(b); there are four regions to consider. In Region I, only a small I_{dc} enters the upper electrode, and $|V_{\text{dc}}|$ is small.

Here, the transition points moved linearly from -100 V (for $P_{\text{high}} = 0$ W) to -350 V (for $P_{\text{high}} = 2000$ W). In Region III, both n_e and I_{dc} changed simultaneously when a bump occurred, which implies that in front of the electrode, they are linked; here, I_{dc} causes a drop in n_e , and $|V_{dc}|$ is large. This occurs when $|V_{dc}|$ is larger than 500 V and $P_{\text{high}} = 2000$ W. In between Regions I and III, we have Region II, where I_{dc} gradually increases with increasing V_{dc} . When a large $|V_{dc}|$ is applied, it is likely that the thickness of the sheath increases due to the high-voltage Child sheath formation, as shown in Fig. 5(b). As a result, the n_e was further depleted in front of the upper electrode, and thus there was a large drop in n_e in Region III.

The electron and the positive ion fluxes are balanced on the electrical floating electrode; the electrical current is given by $I_{dc} = I_i - I_e + I_{se}$, where I_{se} is the secondary electron emission current, I_i and I_e are the electrical current (AeI) collected at an electrode of area A , and the subscripts i and e indicate ions and electrons, respectively. Note that I_{dc} is due to the incidence of positive ions that are accelerated by the applied negative potential and the secondary emission of electrons due to the impact of the ions. As $|V_{dc}|$ increased, the n_e dependence became that of Region IV; however, there were no clear I_{dc} transition behaviors.

Table II summarizes the results for n_e and I_{dc} ; the relationship between n_e and I_{dc} is shown for each region. In particular, in Region II, we note that the increase in n_e is due to the superposition of V_{dc} , I_{dc} , and the saturated I_{dc} , and it increases gradually. A further increase in V_{dc} results in a small increase in I_{dc} .

The following is a summary of the experimental results presented above:

- 1) There is a monotonic increase in the electron density n_e when P_{high} is increased.
- 2) The depletion width W_s at the lower electrode was wider than that at the upper

electrode. The location of the maximum moves in the direction of the lower electrode.

- 3) When no P_{low} is applied, the bulk n_e decreases when V_{dc} is applied.
- 4) The bulk n_e increases only when a large P_{low} is applied.
- 5) The depletion width at the upper electrode becomes wider when large P_{high} is applied.
- 6) V_{dc} first increases with n_e (Region II), then decreases (Region III), and finally increases linearly (Region IV).
- 7) I_{dc} is detectable when V_{dc} is applied. In Regions II and III, I_{dc} gradually increases with $|V_{\text{dc}}|$ and then becomes almost constant in Region IV. I_{dc} increases only slightly with I_{se} .

5. Discussion

5-1. Single-frequency CCP with V_{dc} superposition

The spatial profile in which $W_s^{\text{lower}} \gg W_s^{\text{upper}}$ can be interpreted as showing an interdependence among the voltages, capacitances, and depletion widths (e.g., $V_s \sim 1/C_s \sim W_s$), and P_{high} distributes the capacitances in an equivalent circuit, as shown in Fig. 1(b). The vhf power P_{high} is applied only to the upper electrode. Here, in the stochastic heating mode, the sheath dynamics appear at the boundaries of both the upper and lower electrodes. As shown in Fig. 1(b), the voltages result in a division of the capacitance. The result is that the capacitance of the lower electrode might be smaller than that of the upper electrode. Since the lower electrode had an electrostatic chucking system, C_{lower} should be lower than C_{upper} , and thus the voltage drop between the lower sheath and the lower blocking capacitor was large.

We note that when a small $|V_{dc}|$ was applied, the I_{dc} was negligible. This means the electron and ion fluxes onto the electrodes were balanced by the electrically floating walls. As $|V_{dc}|$ increased, we observed a gradual increase in I_{dc} , and the voltages were within a range of 100 V. The dc superposition appears to have changed the potential of the sheath edge. The electron loss at the wall was the most important factor in determining n_e , and the electron generation increased with increasing heating due to the P_{high} input. The flow of I_{dc} in the upper electrode simultaneously increases Γ_e at the other electrodes. The electrically connected ground acts as an electron sink, and the electrically floated electrode is charged by positive ions; it is thus instantaneously neutralized.

We now review the previously published computational results. Kawamura *et al.* reported results for particle-in-cell (PIC) Monte Carlo collision (MCC) calculations for the superposition of dc and rf at symmetrical CCP discharges [32,33]. They focused on the secondary electron emissions at the dc superposed electrode and considered different values for the secondary electron emission coefficient, γ . When there was only an rf discharge, the pressure was 45 mTorr with Ar at 4 MHz, and it was assumed to be a collisional case; they observed that the rf portions of the sheath lengths decreased as the density at the sheath edge increased. In the dc/rf combination case, the density is significantly asymmetric, with the density at the sheath edge a factor of 1.6 larger than that near the dc/rf electrode. The source of this asymmetry is the excess ionization from the higher-energy secondary electrons, which deposit most of their energy near the sheath.[32,33] As the pressure decreased to 10 mTorr, the plasma became nearly symmetric, with approximately the same integrated density in all areas; the increase in the diffusion losses due to the larger sheath width at the dc electrode (smaller bulk

plasma width) were compensated by the increase in discharge efficiency of the secondary electrons. The secondary electrons do not significantly perturb the symmetry, because most of them are absorbed.[32,33] This is a nontraditional γ mode, and it differs from the traditional γ mode, which is sustained by secondary electrons that appear in the dc discharge.

For the experimental apparatus used in this study, we cannot rigorously analyze the symmetry of the spatial distribution, but we can note that the observed symmetry was consistent with the computational results. The abnormal γ mode for the rf/dc combination with high $|V_{dc}|$ was confirmed experimentally; that is, our experimental results were qualitatively supported.

5-2. Dual-frequency CCP with V_{dc} superposition

The stochastic heating for the dual-frequency CCP should be taken into account when independently forming a more complicated sheath in front of each electrode. Chabert and Braithwaite noticed that due to the instantaneous overlap of two frequencies, the sheath position oscillates, and consequently, the maximum extent of the collisional sheath s_m is determined.[29] Note that s_m is inversely proportional to the driving frequency.[29] When vhf power (60 MHz) was applied to the upper electrode, the sheath thickness was thinner than it was when rf power (13 MHz) was applied to the lower electrode.

From our results, it is unclear whether the heating mode is collisional or collisionless. The operating frequencies have been considered by various researchers. Abdel-Fattah and Sugai reported a transition to electron heating mode from collisional

ohmic heating at low frequencies for plasma surface heating in the VHF range.[65] Sahu and Han reported both ohmic and stochastic modes in a dual-frequency (13 and 320 MHz) CCP in the relatively low-pressure regime (30 Pa).[66] Turner discussed collisional ohmic heating in the bulk and in the sheath.[67-71] The other mode is momentum transfer from the edge of a high-voltage sheath; this is known as collisionless stochastic heating. Kawamura *et al.* considered electron heating modes in CCP.[72,73] Lafleur *et al.* reported computational results that showed that in multiple-frequency discharges, the total electron heating comprises collisional (ohmic) and pressure heating, and they observed an additional collisionless heating mechanism associated with electron inertia.[74] At high pressure, bulk plasma density abruptly increases following the transition, and the average electron energy drops to that sustained by secondary electrons when high dc voltages continue to be applied.[75] At low pressure, there is stochastic heating while the dc voltage increases, although the overall heating power decreases; ohmic heating is also observed.[75] As a result, when no V_{dc} is applied, the experimental results indicated that stochastic heating is dominant.

Denpoh and Ventzek reported the results of a method for tracing test particles.[34,35] In a two-frequency CCP setup for CF_4 discharges, the upper electrode received overlapped dc and vhf power (60 MHz), and the lower electrode received rf power (2 MHz); they showed that the sheath thickness increased in front of the upper electrode, and the bulk electron density increased.[34,35] If rf power was supplied to the lower electrode, the sheath potential in front of that electrode repelled electrons; this action was lost if the rf power was removed. Our experimental results supplied further evidence for this. Thus, we again emphasize the importance of the rf supply at the lower electrode; it serves as a counter electrode for the dc superposed electrode and increases

the bulk n_e and the emission of secondary electrons at the upper electrode.

Zhang *et al.* considered a PIC calculation for CF_4 ; the upper electrode received vhf power (60 MHz) and dc, and the lower electrode received rf power (2 MHz).[44,45, 76-78] When no dc bias is applied, the discharge is primarily maintained by the dual-frequency coupling effect. When applying a superposed dc voltage, the plasma density first increases, then decreases, and finally increases again.[44] They explained that this results in the transition between the four main heating modes: dual-frequency coupling, dc and dual-frequency coupling, dc source-dominant heating, and secondary electron dominant heating.[44] When the dc superposed and dc self-bias voltages are comparable, the coupling effect of dc and rf dominates the heating mechanism, and causes an increase in the plasma density. Depending on the balance between the voltages, the electron trapping in the bulk region is weakened, and hence the plasma density decreases. Finally, when the dc voltage is sufficiently large, the high-energy secondary electrons originating at the dc electrode contribute most of the ions, and this gives rise to another increase in the plasma density.[44]

The ionization rate can be estimated from the optical emission intensity of the excited gas. Gans *et al.* reported phase-resolved optical emission spectroscopic (PROES) observations of spatiotemporal electron-induced excitation. [79-81] In the future, a similar experiment is needed to determine the heating mode transition when there is a low-pressure discharge; the dc superposed dual-frequency CCP may show the spatiotemporal variation of the excitation rate. Very recently, Liu *et al.* reported that strong modulations in the plasma density and light emissions known as “striations” were observed in electronegative capacitively coupled rf (CCRF) plasmas.[82] They suggest that these striations are generated by the resonance between the driving radio

frequency and the ion-ion eigenfrequency, and that this modulates the electric field, the ion densities, and the energy gain and loss processes of the electrons in the plasma.[82] They pointed out that this is very sensitive to the species of ion, such as ions in O₂, SF₆, or C₄F₈ gas[82]; therefore, the disturbance in the electronegativity can be ignored in this case, because of the abundant dilution of Ar. However, such a detailed experiment is a topic for future investigation.

5-3. Currents in the upper electrode, I_{dc}

In the dc superposition that induced the secondary emission of electrons at the dc electrode surface, the I_{dc} was observed experimentally in order to determine the mode transition. However, we should note that the complete relationship between n_e and I_{dc} was not determined. When a large |V_{dc}| is applied, I_{dc} can be used to monitor of strength of n_e, since it is closely related to the ion fluxes of the substrate. If we assumed the ion specie was Ar⁺ and that they had an electron temperature T_e of 5 eV, then an I_{dc} of 1.11 mA cm⁻² predicted an n_e of 0.4×10¹¹ cm⁻³. The measured n_e was 1.6×10¹¹ cm⁻³, which was approximately consistent with I_{dc}, since it is only off by a factor of four. Thus, this approach can be used to obtain a rough estimate of n_e.

In Region II, when an intermediate dc bias was applied (i.e., between -300 and -600 V), the bulk n_e was reduced. As the dc voltage further increased, the discharge gradually switched from the stochastic mode (α) to the mode dominated by secondary electrons (γ). As the accelerating ions impinge onto the upper electrode surface, the secondary electrons are emitted from the surface. The secondary emissions are dependent on the striking energy of the ions, and the secondary emission coefficients

ranged from 0 to 0.1. The secondary electrons approaching the sheath are repelled when the sheath potential exceeds the upper electrode sheath potential. Region II then appears with a gradual rise in I_{dc} , which reflects the amplitude of the secondary emissions due to impinging ions accelerated by the sheath potential. Note that the self-biased voltages applied at the upper electrode (for vhf power) were approximately -200 V for $P_{high} = 800$ W, and the fluctuations were roughly 100 V.

5-4. Spatial profiles of n_e for V_{dc} superposition

In the above discussion, we summarized the effects of the dc superposition on the dual-frequency CCP in terms of the dc self-bias, the transition of the heating mode from α to γ , and the secondary electron emissions from the dc-biased surface.

As $|V_{dc}|$ increases, n_e first increases, then decreases, and finally increases again. This behavior was first reported by Yamaguchi *et al.* [8] and later by Zhang *et al.* [39,40]. When a high P_{low} (1500 W) was applied to the lower electrode and the V_{dc} increased, they observed the following: as V_{dc} increased further, n_e decreased.

We modeled the bulk plasma density and its spatial profile when the dc was superposed in the dual-frequency CCP. Figure 8 shows a schematic of the model. Without the application of P_{low} , electrons do not remain in the bulk plasma, and these results in them being lost to the lower electrode. This is consistent with Kawamura's computational results.[28,29]

For high secondary emissions, it was necessary that the accelerated ion energies exceed 500 V; the heating then moved to the γ mode if V_{dc} was sufficiently larger than -500 V. Importantly, if the sheath potential of the counter electrode, opposite

the electrode to which V_{dc} was applied, was less than that at the upper electrode, then the electrons are not trapped in the bulk plasma region. This means that the applied V_{dc} increases the loss of electrons when they recombine at the wall. This is why we began by experimentally determining the spatial profile of n_e when V_{dc} is applied in a dual-frequency capacitive coupled discharged plasma.

We also wish to consider the emission of secondary electrons. When the high-energy electrons impact the surface of the lower electrode, they provide a dc bias superposition. The apparently large potential of the sheath in front of the upper electrode accelerates the electrons that are emitted. When P_{low} is small, it has low self-bias, and the secondary electrons pass through the sheath in front of the lower electrode. However, when the self-bias is high at the lower electrode, the secondary electrons are unable to overcome the barriers of the sheath potential. This implies there is no neutralization of the charge of hot electrons in the microstructures of the lower electrode.

6. Conclusions

In a dc superposed dual-frequency CCP apparatus, we used an SW probe to experimentally measure the interelectrode electron density profile under conditions encountered in practice and using the electronegative gas of C_4F_8 . By changing the position of the probe, we were able to measure changes in the spatial profile when a negative dc bias was applied to the upper electrode. When rf power was applied to the lower electrode, the sheath potential there changed the spatial profile and increased the bulk electron density. When the rf power at the lower electrode was as large as the

potential of the sheath at the upper electrode, the secondary electrons were trapped. We suspected that the spatial profile of n_e reflected the blocking capacitors and the transition of the heating mode from α to γ . The heating mode was changed when the secondary electron emissions accelerated due to the high-voltage sheath; it is possible that part of this may be ballistic transport to the counter electrode, thereby neutralizing the local surface charge. This can be summarized by saying that the heating of the secondary electrons was dominated by transitions from the α mode to the γ mode. At the voltage at which this transition occurs, the negative dc bias causes a characteristic bump in the bulk n_e . The application of the negative dc bias maintains or slightly decreases the n_e , but as the voltage reaches that of the counter sheath potentials, which fluctuate by hundreds of volts, n_e increases. Thus, the dc superposition affects the spatial profile of n_e only when there is a large rf power on the lower electrode.

Acknowledgement

The author thanks Prof. H. Sugai of Chubu University; Drs. K. Denpoh and P. Ventzek of Tokyo Electron America, Ltd.; M. Tomura and M. Iwata of Tokyo Electron Miyagi, Ltd.; and T. Tsutsumi and T. Ueyama of Nagoya University for fruitful discussions.

References

- 1) N. Hosokawa, R. Matsuzaki and T. Asamaki, Japan. J. Appl. Phys. 13 (1974) 435.
- 2) H. Abe, M. Yoneda, and N. Fujiwara, Japan. J. Appl. Phys. 47 (2008) 1435.
- 3) K. Nojiri, "*Dry Etching Technology for Semiconductors*", (Springer, 2015).
- 4) H. H. Goto, H-D. Lowe, and T. Ohmi, J. Vac. Sci. Technol. A 10 (1992) 3048.
- 5) V. Vahedi, C. K. Birdsall, M. A. Lieberman, G. DiPeso, and T. D. Rognlien, Phys. Fluid. B 5 (1993) 2719.
- 6) W. Tsai, G. Mueller, R. Lindquist, B. Frazier, and V. Vahedi, J. Vac. Sci. Technol. B 14 (1996) 3276.
- 7) T. Tatsumi, M. Matsui, M. Okigawa, M. Sekine, J. Vac. Sci. Technol. B 18 (2000) 1897.
- 8) M. Sekine, Appl. Surf. Sci. 192 (2002) 270.
- 9) M. Nagai, M. Hori, and T. Goto, Japan. J. Appl. Phys. 43 (2004) L501.
- 10) M. Nagai, and M. Hori, Japan. J. Appl. Phys. 46 (2007) 1176.
- 11) T. Yamaguchi, T. Kimura, C. Koshimizu, K. Takeda, H. Kondo, K. Ishikawa, M. Sekine and M. Hori, Japan. J. Appl. Phys. 50 (2011) 056101.
- 12) T. Yamaguchi, T. Komuro, C. Koshimizu, S. Takashima, K. Takeda, H. Kondo, K. Ishikawa, M. Sekine, and M. Hori, J. Phys. D: Appl. Phys. 45 (2012) 025203.
- 13) Y. Miyawaki, Y. Kondo, M. Sekine, K. Ishikawa, T. Hayashi, K. Takeda, H. Kondo, and M. Hori, Japan. J. Appl. Phys. 52 (2013) 016201.
- 14) T. Suzuki, K. Ishikawa, K. Takeda, H. Kondo, M. Sekine, and M. Hori, J. Phys. D: Appl. Phys. 47 (2014) 422002.
- 15) Y. Kondo, Y. Miyawaki, K. Ishikawa, T. Hayashi, K. Takeda, H. Kondo, M. Sekine, and M. Hori, J. Phys. D: Appl. Phys. 48 (2015) 045202.

- 16) Y. Kondo, K. Ishikawa, T. Hayashi, Y. Miyawaki, K. Takeda, H. Kondo, M. Sekine, and M. Hori, *J. Appl. Phys.* 54 (2015) 040303.
- 17) Y. Ohya, M. Tomura, K. Ishikawa, M. Sekine, and M. Hori, *J. Vac. Sci. Technol. A* 34 (2016) 040602.
- 18) W. T. Lai, C. J. Hwang, A. T. Wang, R. Hwang, J. C. Yau, J. Liao, L. H. Chen, K. Adachi, and S. Okamoto, *Proc. Intern. Symp. on Dry Process*, (Institute of Electrical Engineers, Japan, 2006).
- 19) T. Nozawa, T. Kinoshita, T. Nishizuka, A. Narai, T. Inoue, and A. Nakaue, *J. Appl. Phys.* 34 (1995) 2107.
- 20) T. Kinoshita, M. Hane, and J. P. McVittie, *J. Vac. Sci. Technol. B* 14 (1996) 560.
- 21) H. R. Koeng and L. I. Maissel, *IBM J. Res. Dev.* 14 (1970) 168.
- 22) K. Kohler, J. W. Coburn, D. E. Horne, E. Kay, and J. H. Keller, *J. Appl. Phys.* 57 (1985) 59.
- 23) U. Czarnetzki, J. Schulze, E. Schungel, and Z Donko, *Plasma Sources Sci. Technol.* 20 (2011) 024010.
- 24) D. Bohm, "*The Characteristics of Electrical Discharges in Magnetic Fields*", ed. A. Guthry and R. K. Wakerling (McGrawhill, New York, 1949).
- 25) K-U. Riemann, *J. Phys. D: Appl. Phys.* 24 (1991) 492.
- 26) see Electromagnetics textbook; for example, J. D. Jackson, "*Classical electrodynamics*", 3rd ed. (Wiley, 1999).
- 27) B. G. Heil, U. Czarnetzki, R. P. Brinkmann, and T. Mussenbrock, *J. Phys. D: Appl. Phys.* 41 (2008) 165202.
- 28) C. W. Coburn, and E. Kay, *J. Appl. Phys.* 43 (1972) 4965.
- 29) P. Chabert and N. Braithwaite, "*Physics of Radio frequency plasmas*" (Cambridge

University Press, Cambridge, 2011).

- 30) K. Yamamoto, and T. Okuda, Appl. Sci. Res. 5 (1956) 144.
- 31) Z. Hassan, and H. Fujita, J. Phys. D: Appl. Phys. 31 (1998) 2281.
- 32) E. Kawamura, M. A. Lieberman, A. J. Lichtenberg, and E. A. Hudson, J. Vac. Sci. Technol. A 25 (2007) 1456.
- 33) E. Kawamura, A. J. Lichtenberg, and M. A. Lieberman, Plasma Sources Sci. Technol. 17 (2008) 045002.
- 34) K. Denpoh and P. L. G. Ventzek, J. Vac. Sci. Technol. A 26 (2008) 1415.
- 35) P. L. G. Ventzek and K. Denpoh, J. Vac. Sci. Technol. A 27 (2009) 287.
- 36) M. A. Lieberman and A. J. Lichtenberg, "*Principles of Plasma Discharges and Materials Processing*" 2nd ed. (Wiley, New Jersey, 2005).
- 37) P. Belenguer, and J. P. Boeuf, Phys. Rev. A 41 (1990) 4447.
- 38) V. A. Godyak, R. B. Piejak, Phys. Rev. Lett. 65 (1986) 996.
- 39) V. A. Godyak, N. Sternberg, Phys. Rev. A 42 (1990) 2299.
- 40) M. A. Lieberman, IEEE Trans. Plasma Sci. 16 (1988) 638.
- 41) S.M. Levitskii, Zh. Tekh. Fiz. 27 (1957) 1001. [Sov. Phys. Tech. Phys. 2, 887 (1957)].
- 42) V. Lisovskiy, J.-P. Booth, K. Landry, D. Douai, V. Cassagne, and V. Yegorenkov, Phys. Plasma 13 (2006) 103505.
- 43) Z. Donko, J. Schulze, B. G. Heil, U. Czarnetzki, J. Phys. D: Appl. Phys. 42 (2009) 025205.
- 44) Q-Z. Zhang, Y-X. Liu, W. Jiang, A. Bogaerts, and Y-N. Wang, Plasma Sources Sci. Technol. 22 (2013) 025014.
- 45) Q-Z. Zhang, Y-N. Wang, and A. Bogaerts, J. Appl. Phys. 115 (2014) 223302.

- 46) J. P. Chang and J. W. Coburn, *J. Vac. Sci. Technol. A* 21 (2003) S145.
- 47) K. Hashimoto, *Japan. J. Appl. Phys.* 33 (1994) 6013.
- 48) K. Hashimoto, *Japan. J. Appl. Phys.* 32, (1993) 6109.
- 49) M. Wang and M. J. Kushner, *J. Appl. Phys.* 107 (2010) 023308.
- 50) M. Wang and M. J. Kushner, *J. Appl. Phys.* 107 (2010) 023309.
- 51) A. V Khrabrov, I. D. Kaganovich, P. L. G. Ventzek, A. Ranjan, and L. Chen, *Plasma Sources Sci. Technol.* 24 (2015) 054003.
- 52) L. Xu, L. Chen, M. Funk, A. Ranjan, M. Hummel, R. Bravenec, R. Sundararajan, D. J. Economou, and V. M. Donnelly, *Appl. Phys. Lett.* 93 (2008) 261502.
- 53) P. Diomedede, S. Longo, D. J. Economou, and M. Capitelli, *J. Phys. D: Appl. Phys.* 45 (2012) 175204.
- 54) H. Kokura, K. Nakamura, I. V. Ghanashev, and H Sugai, *Japan. Appl. Phys.* 38 (1999) 5262.
- 55) H. Sugai, I. Ghanashev, M. Hosokawa, K. Mizuno, K. Nakamura, H. Toyoda and K. Yamauchi, *Plasma Sources Sci. Technol.* 10 (2001) 378.
- 56) H. Sugai, *J. Plasma Fusion Res.* 78 (2002) 998.
- 57) K. Ishikawa, S. Hayashi, and M. Sekine, *J. Appl. Phys.* 93 (2003) 1403.
- 58) M. Lapke, T. Mussenbrock, R. P. Brinkmann, C. Scharwitz, M. Böke, and J. Winter, *Appl. Phys. Lett.* 90 (2007) 121502.
- 59) C. Scharwitz, M. Böke, S-K. Hong, and J. Winter, *Plasma Process Polym.* 4 (2007) 605.
- 60) C. Scharwitz, M. Böke, and J. Winter, *Plasma Process Polym.* 6 (2009) 76.
- 61) Y. Ohya, M. Iwata, K. Ishikawa, M. Sekine, and M. Hori, *Japan. J. Appl. Phys.* 55 (2016) 080309.

- 62) B. Li, H. Li, Z. Chen, J. Xie and W. Liu, *J. Phys. D: Appl. Phys.* 43 (2010) 325203.
- 63) J. Schulze, A. Derzsi, K. Dittmann, T. Hemke, J. Meichsner, and Z. Donko, *Phys. Rev. Lett.* 107 (2011) 275001.
- 64) J. Schulze, Z. Donko, E. Schungel, and U. Czarnetzki, *Plasma Sources Sci. Technol.* 20 (2011) 045007.
- 65) E. Abdel-Fattah, and H. Sugai, *Appl. Phys. Lett.* 83 (2003) 1533.
- 66) B. B. Sahu and J. G. Han, *Phys. Plasmas* 23 (2016) 053514.
- 67) M. M. Turner, *Phys. Rev. Lett.* 75 (1995) 1312.
- 68) M. M. Turner, *Plasma Sources Sci. Technol.* 22 (2013) 035014.
- 69) M. M. Turner, *J. Phys. D: Appl. Phys.* 46 (2013) 285203.
- 70) U. Czarnetzki, T. Mussenbrock, and R. P. Brinkmann, *Phys. Plasmas* 13 (2006) 123503.
- 71) M.A. Lieberman, A. J. Lichtenberg, E. Kawamura, T. Mussenbrock and R. P. Brinkmann, *Phys. Plasmas* 15 (2008) 063505.
- 72) E. Kawamura, M. A. Lieberman, and A. J. Lichtenberg, *Phys. Plasmas* 13 (2006) 053506.
- 73) E. Kawamura, M. A. Lieberman, and A. J. Lichtenberg, *Phys. Plasmas* 21 (2014) 123505.
- 74) T. Lafleur, P. Chabert and J. P. Booth, *Plasma Sources Sci. Technol.* 23 (2014) 035010.
- 75) W. Jiang, X. Xu, Z-L. Dai, and Y-N. Wang, *Phys. Plasmas* 15 (2008) 033502.
- 76) Q-Z. Zhang, W. Jiang, S-X. Zhao, and Y-N. Wang, *J. Vac. Sci. Technol. A* 28 (2010) 287.
- 77) Q-Z. Zhang, W. Jiang, L-J. Hou, and Y-N. Wang, *J. Appl. Phys.* 109 (2011) 013308.

- 78) S. Wang, X. Xu, and Y-N. Wang, Phys. Plasmas 19 (2012) 113506.
- 79) T. Gans, C.C. Lin, V. Schulz-von der Gathen and H. F. Döbele, Phys. Rev. A 67 (2003) 012707.
- 80) T. Gans, D. O'Connell, V. Schulz-von der Gathen, and J. Waskoenig, Plasma Sources Sci. Technol. 19 (2010) 034010.
- 81) K. Dittmann, K. Matyash, S. Nemschokmichal, J. Meichsner, and R. Schneider, Contrib. Plasma Phys. 50 (2010) 942.
- 82) Y-X. Liu, E. Schüngel, I. Korolov, Z. Donkó, Y-N. Wang, and J. Schulze, Phys Rev. Lett. 116 (2016) 255002.

Table I. Previous studies of dc/rf combination and dc superposition onto the rf electrode.

Exp: experimentally; and Comp: computationally.

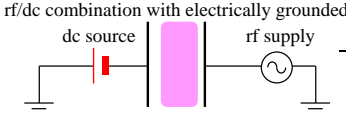
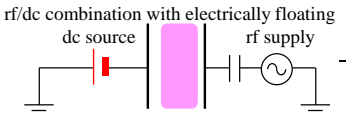
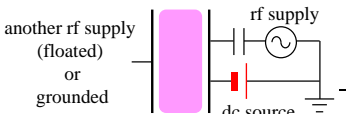
Type	Short description	Ref.
1. rf/dc combination		
	Exp: dc and rf fields perpendicularly superposed Air discharge was reported.	[30]
	Exp: dc CF ₄ or Ar discharge at 1mTorr with modulation of rf (1k-28 MHz) was reported.	[31]
	Comp: combined dc/rf (4-13 MHz) discharge at 60 mTorr (4.5 Pa) was reported. Secondary electron emissions	[32] [33]
	Exp: dc/rf (13.56 MHz) hybrid Ar discharge was reported. Highly energetic electron was measured	[72] [73]
	Comp: dc/rf combined discharge or hybrid dc/rf CF ₄ discharge was reported.	[76- 78]
2. dc superposition onto rf electrode		
	Exp: dc-biased rf (13.56MHz) Ar discharge with the counter grounded were reported. Ion energy measurements were conducted.	[22]
	Comp. hybrid dc/rf (60MHz) discharge with the counter rf bias (2MHz) was reported. Highly energetic electron was calculated.	[34] [35]
	Exp: dc superposed vhf (60MHz) C ₄ F ₈ /N ₂ /Ar discharge at 5.3 Pa with the counter rf bias (13.56 MHz) was reported.	[11] [12]
	Comp: hybrid dc/dual rf (60MHz) CF ₄ discharge at 70mTorr (5.3 Pa) with the counter rf biased (2MHz) was reported.	[44] [45]
	Comp: dc-augmented rf (10-100 MHz) Ar/C ₄ F ₈ /O ₂ discharge with the counter rf bias (1-2MHz) was reported. Ion energy/angle distribution and secondary electron emission were calculated.	[49] [50]

Table II. Plasma characteristics in each V_{dc} region. V: voltages; W: depletion widths; see text for other abbreviations.

Regions	I	II	III	IV
	$V_{dc} < V_s^{\text{upper}}$	$V_{dc} \simeq V_s$	$V_{dc} > V_s$	$V_{dc} \gg V_s$
V_s^{upper}	upper \leq lower		upper $>$ lower	
V_s^{lower}	upper \leq lower		upper $>$ lower	
bulk n_e	const.	\uparrow	\downarrow	$\uparrow\uparrow$
I_{dc}	0	\nearrow	\rightarrow	\nearrow
$W_s^{(\text{upper})}$	upper		upper	
$W_s^{(\text{lower})}$	\wedge lower		\vee lower	
Z^{max}	slightly upper		center	move to lower

Figure captions

- Figure 1 (a,b) Equivalent circuit models of a capacitively coupled plasma (CCP) discharge, (c) time-averaged charged particle density distribution between the electrodes, (d) time-averaged potential between the electrodes. Φ : potential; V : voltage; Γ : flux.
- Figure 2 (a) Schematic of the experimental setup of the dual-frequency capacitively coupled plasma etching reactor, and (b) using the SW probe to measure the interelectrode spatial distribution of electron density.
- Figure 3 Spatial profile of the n_e dependence on the upper vhf power (from 500 W to 2000 W), with and without application of the lower rf power and the upper negative dc bias.
- Figure 4 (a) Dependence of the electron density on the voltage of the dc bias, and (b) spatial profile of the electron density as a function of the interelectrode position when no rf power is applied to the lower electrode.
- Figure 5 Spatial profile of electron density as a function of the interelectrode position for different levels of vhf power: (a) 800 W, and (b) 2000 W.
- Figure 6 Interelectrode electron density as a function of the dc superposition voltage for different levels of vhf power (from 800 W to 1600 W) and different levels of rf power applied to the lower electrode: (a) 800 W, (b) 1500 W, and (c) 2400 W. (d) Electron density surface showing the dependence on the dc bias and the vhf power.
- Figure 7 Dependence on the applied negative dc bias voltage when the rf power was 1500 W for (a) the current density flowing through the upper electrode, and (b) the electron density. Data are shown for vhf power ranging from 800 W to 2000

W.

Figure 8 Proposed model for determining the spatial profile of n_e in a dual-frequency CCP with the superposition of a negative dc bias. (a, c) small P_{low} , and (b, d) high P_{low} ; (a, b) without V_{dc} , and (c, d) with V_{dc} .

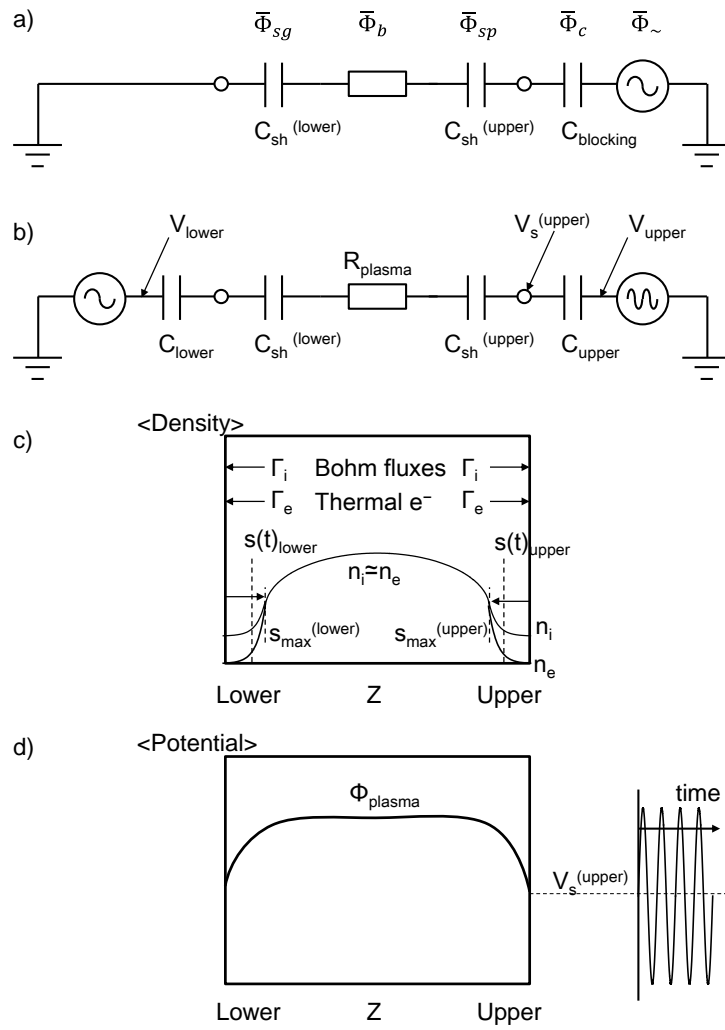


Figure 1

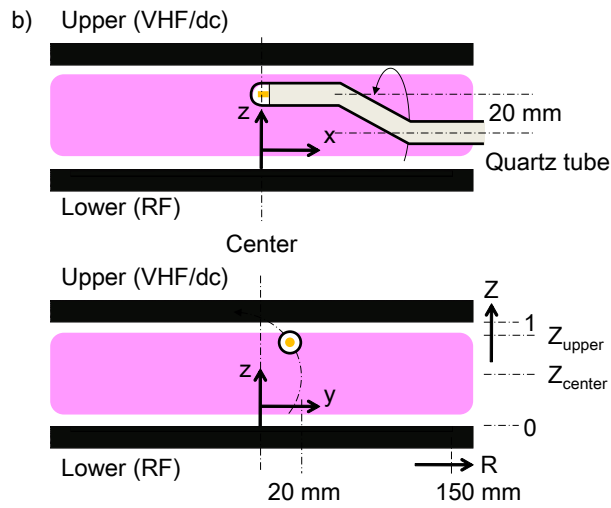
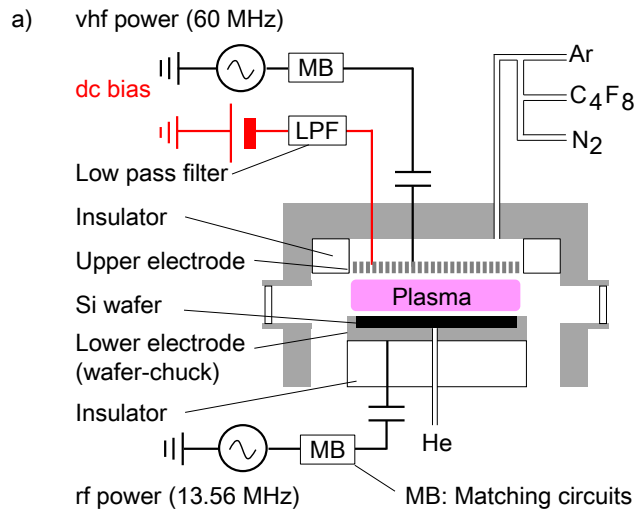


Figure 2

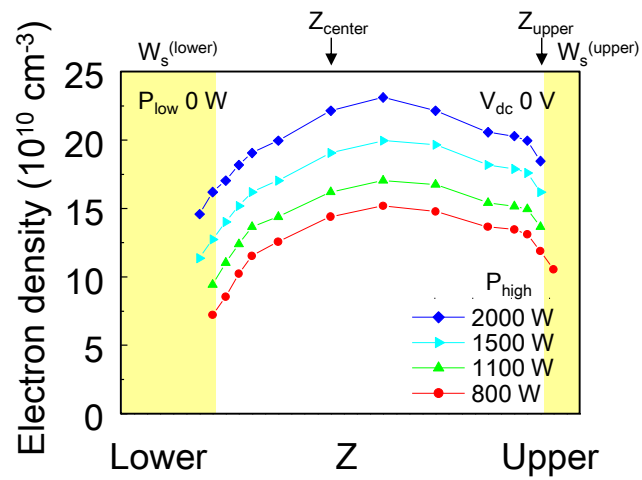


Figure 3

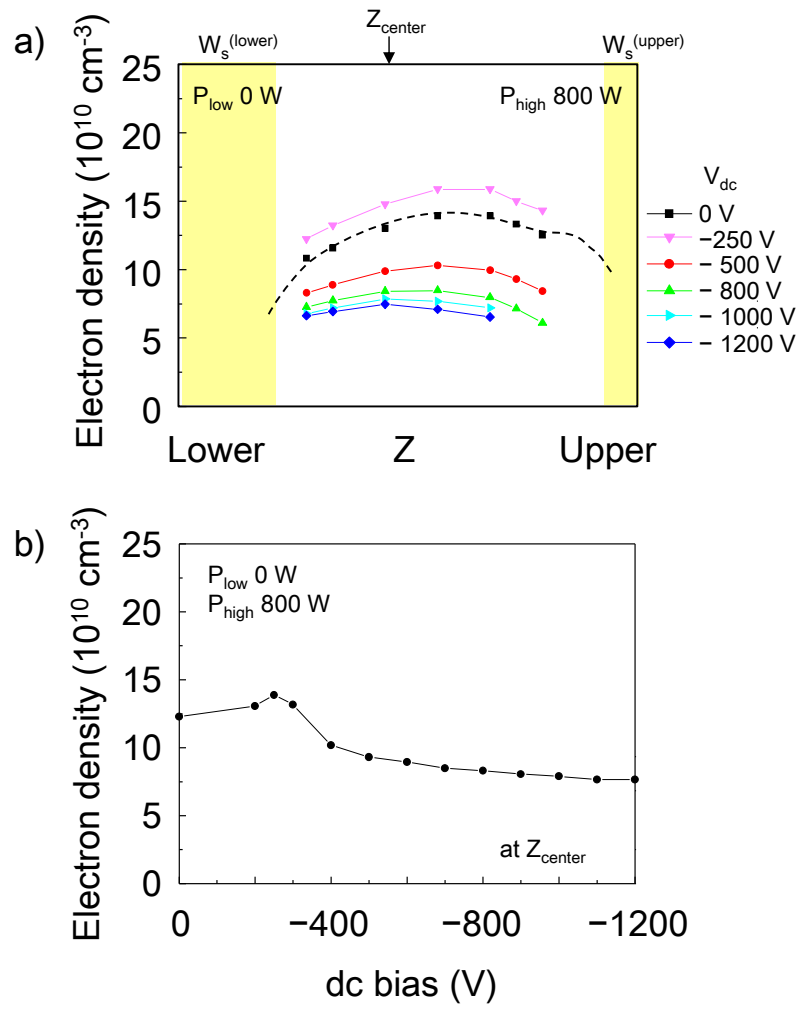


Figure 4

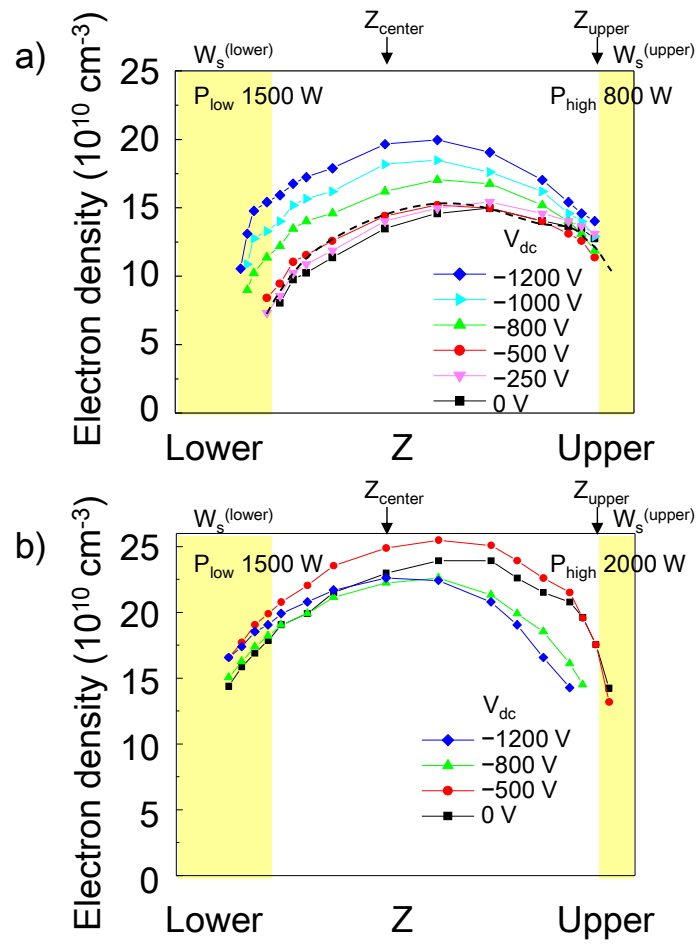


Figure 5

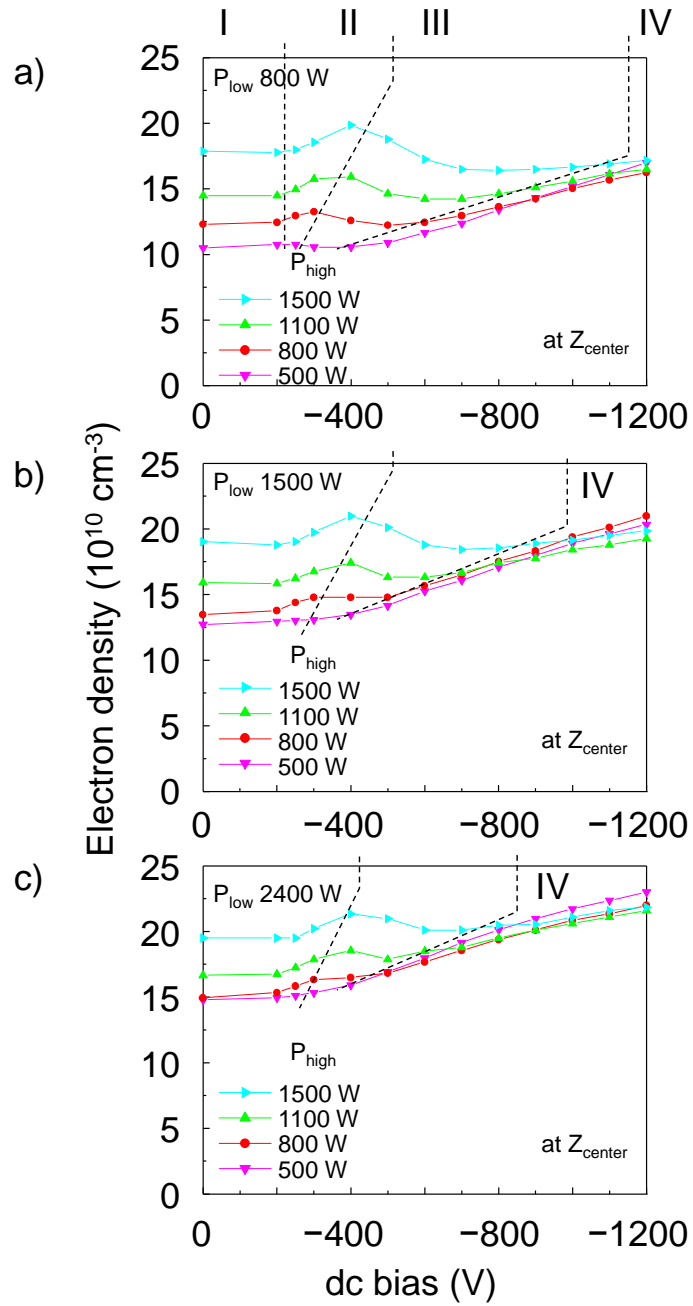


Figure 6

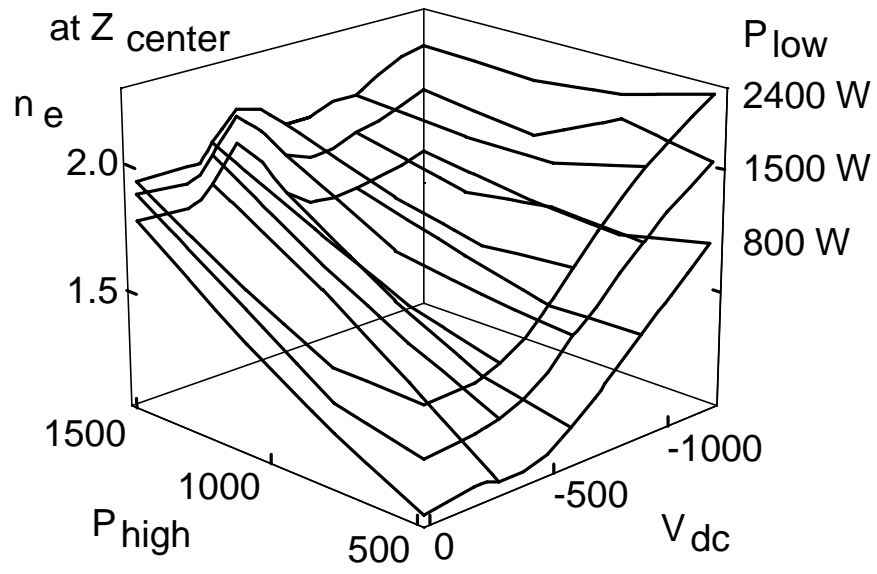


Figure 6 (contd.)

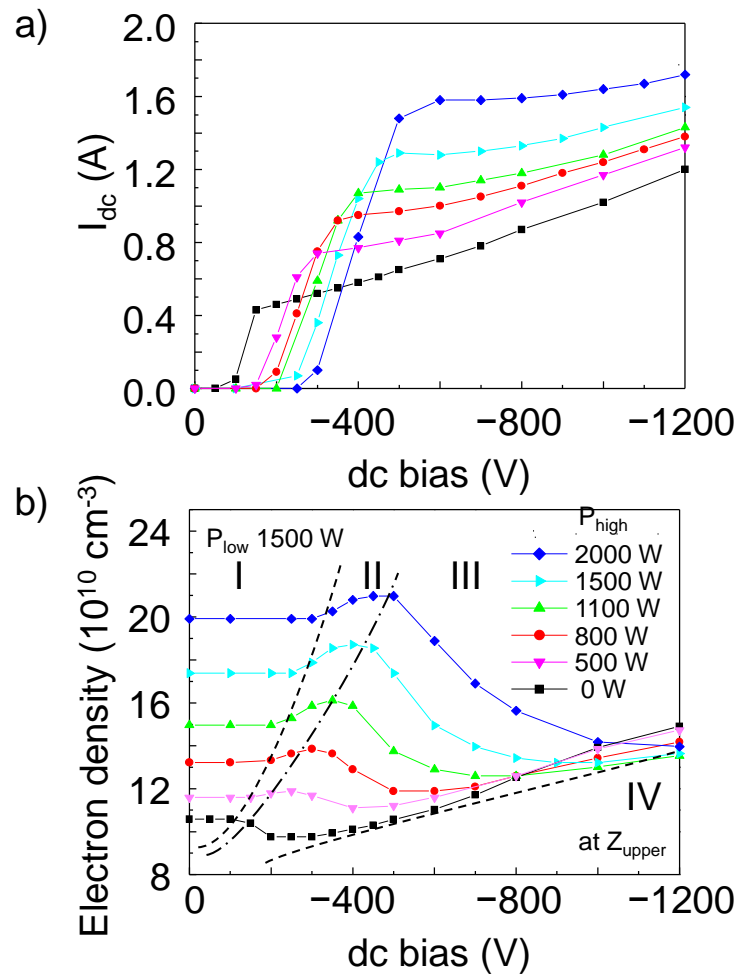


Figure 7

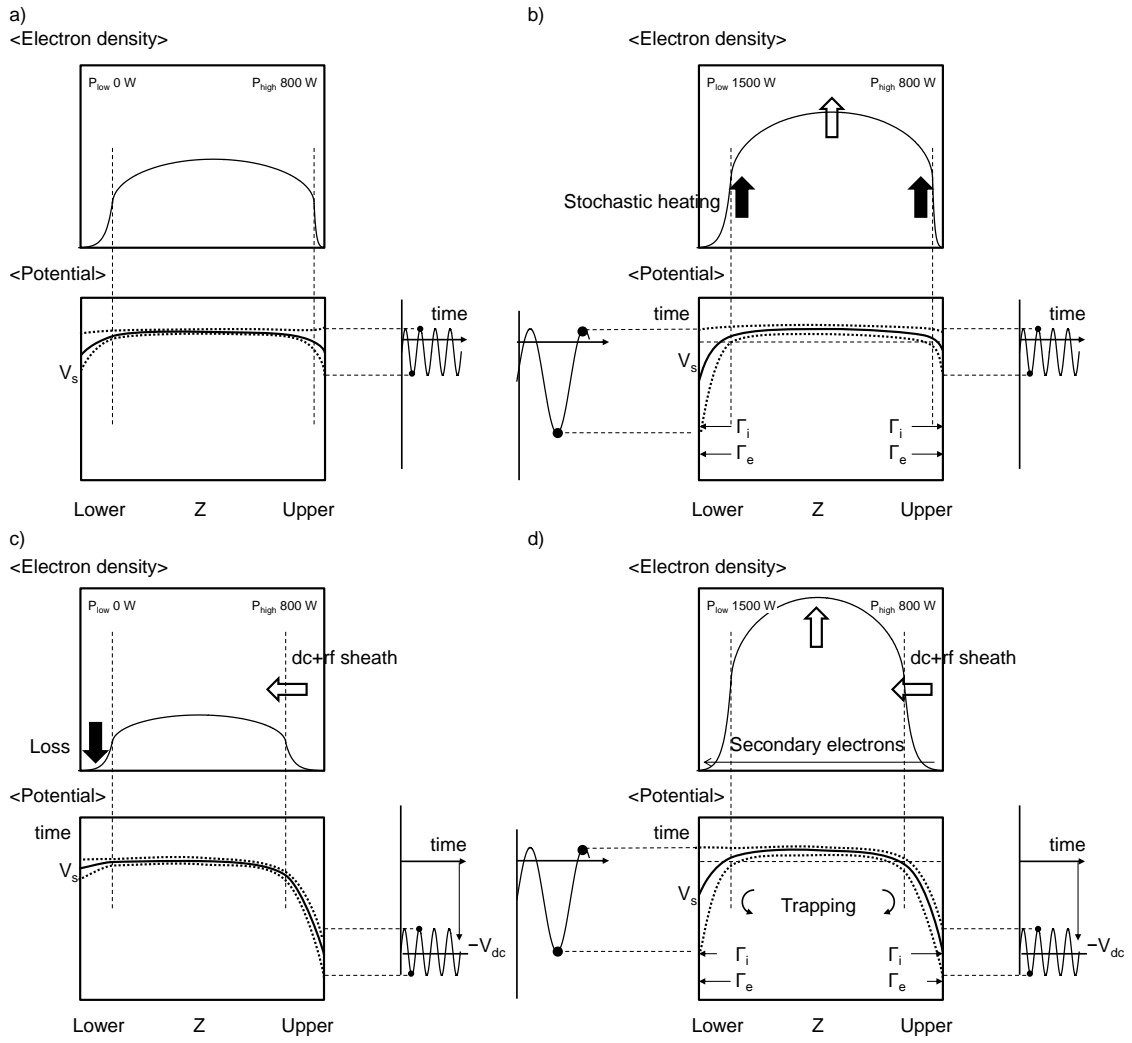


Figure 8